Geophys. J. Int. (2000) **142,** 631–642

Convection in the Earth's core driven by lateral variations in the core–mantle boundary heat flux

Steven John Gibbons[1,2] and David Gubbins[1]

[1] *School of Earth Sciences, University of Leeds, Leeds,* LS2 9JT, *UK*
[2] *School of Mathematical Sciences, University of Exeter, Exeter,* EX4 4QE, *UK. E-mail: S.J.Gibbons@ex.ac.uk*

Accepted 2000 March 31. Received 2000 March 14; in original form 1999 March 4

SUMMARY

Moving core fluid maintains an isothermal core–mantle boundary (CMB), so lateral variations in the CMB heat flow result from mantle convection. Such variations will drive thermal winds, even if the top of the core is stably stratified. These flows may contribute to the magnetic secular variation and are investigated here using a simple, non-magnetic numerical model of the core. The results depend on the equatorial symmetry of the boundary heat flux variation. Large-scale equatorially symmetric (E^S) heat flux variations at the outer surface of a rapidly rotating spherical shell drive deeply penetrating flows that are strongly suppressed in stratified fluid. Smaller-scale E^S heat flux variations drive flows less dominated by rotation and so less inhibited by stratification. Equatorially anti-symmetric flux variations drive flows an order of magnitude less energetic than those driven by E^S patterns but, due to the nature of the Coriolis force, are less suppressed by stratification. The response of the rotating core fluid to a general CMB heat flow pattern will then depend strongly on the subadiabatic temperature profile. Imposing a lateral heat flux variation linearly related to a model of seismic tomography in the lowermost mantle drives flow in a density stratified fluid that reproduces some features found in flows inverted from geomagnetic data.

Key words: convection, core–mantle boundary, geomagnetism, heat flux, stratification, symmetries.

1 INTRODUCTION

Whilst some features of the Earth's magnetic field are observed to be in constant motion (the secular variation or SV), others have been shown to have persisted throughout the historical record (see Bloxham *et al.* 1989 and Hutcheson & Gubbins 1990). Furthermore, the independent studies of Gubbins & Kelly (1993) and Johnson & Constable (1995) showed that the time-averaged fields from the past 5 Myr, analysed from palaeomagnetic databases, are not axially symmetric. Longitudinal persistence of features suggests that conditions at the base of the mantle control the behaviour of the magnetic field, although it is unclear whether the SV results from the main dynamo process or is an effect of independent processes occurring at the top of the core (see e.g. Davis & Whaler 1993).

The effect of the mantle upon core dynamics was proposed by Hide (1967). The first mechanism considered by Hide (1969) was that of topographic coupling, low-order departures from spherical symmetry at the CMB being argued to correlate with non-dipolar components of the magnetic field. The CMB topography is unlikely to be large in magnitude, although large length scales with small lateral variations may be significant in determining the scale of convective motion (Bassom & Soward 1996; Bell & Soward 1996).

Alternatively, core–mantle interaction may be achieved through electromagnetic coupling. Jeanloz (1990), Knittle & Jeanloz (1991) and Li & Jeanloz (1987) suggested that lateral heterogeneity in the conductivity of the lowermost mantle is able to lock or deflect lines of the magnetic field, affecting the field's surface morphology. These large variations in conductivity are explained in terms of the infiltration of core fluid into the lowermost mantle, although Poirier *et al.* (1998) argued that the lateral conductivity variations are insignificant.

The final means of core–mantle coupling is through lateral variations in heat flow across the CMB, which will be studied here. Mantle convection will produce a lateral temperature variation in the lowermost mantle, although the relatively rapid fluid motions of the core will act to make the CMB isothermal, an upper bound of 4×10^{-5} K in lateral temperature variation at the top of the core being suggested by Stacey (1991). Gubbins & Richards (1996) correlated lateral seismic velocity variations and the CMB magnetic field morphology,

and Bloxham & Gubbins (1987) confirmed by an order of magnitude calculation that lateral temperature variations of as little as 1 K in the lowermost mantle could drive thermal wind flows at the top of the core.

Zhang & Gubbins (1992) solved for steady flows driven by lateral variations in temperature at the surface of a rapidly rotating sphere, specifying temperature rather than heat flux for mathematical convenience. In a further study (Zhang & Gubbins 1993), inhomogeneous temperature boundary conditions were imposed in the unstable convection problem and some large-scale, equatorially symmetric heating modes were found to lock flows that would otherwise drift. Sun *et al.* (1994) also applied inhomogeneous cooling to the surface of a convecting shell but, unlike Zhang & Gubbins (1993), at highly supercritical Rayleigh number. In this case, flow in the outer part of the shell was found to lock to the surface inhomogeneity, with flow towards the centre being relatively unaffected. However, only two patterns of thermal inhomogeneity were examined and, again for numerical simplicity, the boundary temperature and not the heat flux was specified.

Olson & Glatzmaier (1996) argued that, in the presence of an imposed magnetic field, even with a lateral heat flux variation 10 times the mean heat flux, flow fails to lock to the boundary and is dominated by the effects of rotation. The full geodynamo simulation of Glatzmaier & Roberts (1997) did not report locking with an inhomogeneous heat flux boundary condition but suggested that the thermal boundary imposed by the mantle may control the frequency of polarity reversals. The enormous computational expense of these calculations, however, means that a very small parameter space can be investigated and so the physical mechanisms involved are difficult to identify. Using a two-mode approximation, Sarson *et al.* (1997) showed locking to occur in a time-average sense only if the thermal inhomogeneity was weak; full locking of flow and field occurred for stronger heat flux variations. Increasing the scale of the heterogeneity further can lead to significant alteration of the boundary-driven flow by the magnetic field, paradoxically weakening the locking.

There is clearly still much to be gained from studying boundary driven flow in isolation. A larger accessible parameter space allows the response of the core to many different geometries of thermal heterogeneities to be explored as a function of the strength of the laterally varying heat flux and core density profile. Although the calculations are non-linear, and therefore expensive in terms of memory, steady flows exist for arbitrarily small lateral heat flux variations, avoiding the need for costly time integrations that seriously limit the available parameter space. The case where boundary-driven flow competes with free convection is dealt with in Gibbons (1998) and a companion paper in preparation. The sensitivity to initial conditions of magnetic calculations (Sarson *et al.* 1997) also suggests that a far greater parameter space must be investigated before firm conclusions can be made as to how boundary heterogeneities affect the dynamo. The lack of magnetic field is clearly a limitation in our present model, but it is important to understand this problem first. Furthermore, the Lorentz force may be insignificant for flow close to the surface in the outer core (Le Mouël 1984).

The top of the core may or may not be stably stratified. Gubbins *et al.* (1982) and Labrosse *et al.* (1997) presented thermal models for the formation of such a layer, whilst Fearn & Loper (1981) and Braginskii (1984, 1993) suggested compositional stratification. The models of Lister & Buffett (1998) accommodate both thermal and compositional stratification. The strength of stable stratification is measured by the Brunt–Väisälä frequency, which can in principle be determined from seismology (see Gubbins & Roberts 1987), although Masters (1979) found the determination of density from the normal mode oscillations insufficiently sensitive. Lay & Young (1990) found differential traveltimes for *S*, *SKS* and *SKKS* waves to be consistent with a stratified layer in the uppermost 50–100 km of the outer core. Geomagnetism has also produced some evidence for such a layer. Lloyd & Gubbins (1990) inverted SV data under the assumption of purely toroidal flow and found that the radial shear decreased with depth on a vertical length scale of about 600 km, consistent with a density stratified layer that inhibits poloidal flow. Whaler (1980) suggested the strong probability of stable stratification at the top of the core in the light of geomagnetic evidence for an absence of upwelling, although further work (Whaler 1984, 1986) has cast doubt on these conclusions, indicating that purely toroidal flows did not match SV data sufficiently well. Gubbins (1991) suggested that surface flow would need to penetrate to a depth of the order of 100 km in order to drive the magnetic secular variation.

The work presented here will extend that of Zhang & Gubbins (1992) by replacing the fixed temperature boundary with the more geophysically realistic fixed heat flux condition. In addition, heat flux patterns that satisfy either equatorial antisymmetry or no reflectional symmetry will be investigated. The effect of using rigid boundary conditions and finite Prandtl number are briefly investigated.

2 FORMULATION

In the following work, r, θ and ϕ are the standard spherical polar coordinates. Boussinesq fluid is contained in an impenetrable spherical shell, where r_i and r_o are respectively the inner and outer radii. The length scale, d, is taken to be the thickness of the shell, $r_o - r_i$, and the aspect ratio, $\eta = r_i/r_o$, is taken to be 0.4, allowing direct comparison with the results of Zhang & Gubbins (1992). The acceleration due to gravity, $\mathbf{g}$, is given in terms of the radial vector, $\mathbf{r}$, by

$$\mathbf{g} = -\gamma \mathbf{r}\,, \tag{1}$$

where γ is a constant. Following the formulation of Zhang & Gubbins (1992), the temperature, T, is expressed as

$$T(r, \theta, \phi, t) = T_0(r) + T_1(r, \theta, \phi, t)\,, \tag{2}$$

where T_0 is a conduction temperature profile satisfying

$$\nabla T_0 = \beta \mathbf{r}\,, \tag{3}$$

which here provides a simple form of density stratification. T_1 is a departure from the reference temperature that satisfies the boundary conditions

$$T_1(r_i) = 0 \tag{4}$$

and

$$\left.\frac{\partial T_1}{\partial r}\right|_{r_o} = \mathscr{H} g(\theta, \phi)\,, \tag{5}$$

where $\mathscr{H}$ is a scale for the lateral variation in the temperature gradient and $g(\theta, \phi)$ defines the lateral dependence of the heat flux, with the normalization condition

$$\int_0^{2\pi} \int_{-\pi}^{\pi} [g(\theta, \phi)]^2 \sin\theta d\theta d\phi = 1 . \tag{6}$$

The boundary conditions on the temperature are made homogeneous by the transformation

$$T_1(r, \theta, \phi, t) = \Theta(r, \theta, \phi, t) + f(r) g(\theta, \phi) , \tag{7}$$

where $f(r)$ is chosen with the properties

$$f(r_i) = 0 , \quad \left.\frac{\partial f}{\partial r}\right|_{r_o} = \mathscr{H} \tag{8}$$

and Θ then satisfies

$$\Theta(r_i) = \left.\frac{\partial \Theta}{\partial r}\right|_{r_o} = 0 . \tag{9}$$

Although the appropriate boundary condition for the Earth's core is that of fixed heat flux, the alternative fixed-temperature outer boundary condition employed by Zhang & Gubbins (1992),

$$T_1(r_o) = \mathscr{T} g(\theta, \phi) , \tag{10}$$

was also coded in order to validate the numerical calculations by reproducing the results of Zhang & Busse (1987) and Zhang & Gubbins (1993).

Scaling length, temperature and time, denoted respectively by d, $\mathscr{H} d$ and d^2/κ (the thermal diffusion time with κ the thermal diffusivity), allow the vorticity and heat equations to be written in the dimensionless forms

$$\frac{E}{P_r} \nabla \times D_t \mathbf{v} = B \nabla \times [\Theta + f(r) g(\theta, \phi) \mathbf{r}] - \nabla \times (\mathbf{k} \times \mathbf{v}) + E \nabla \times \nabla^2 \mathbf{v} \tag{11}$$

and

$$\frac{\partial \Theta}{\partial t} + S_t \mathbf{v} \cdot \mathbf{r} = \nabla^2 [\Theta + f(r) g(\theta, \phi)] - \mathbf{v} \cdot \nabla [\Theta + f(r) g(\theta, \phi)] , \tag{12}$$

where $\mathbf{v}$ is the fluid velocity, $\mathbf{k}$ is the unit vector along the rotation axis and D_t is the fluid derivative given by

$$D_t = \frac{\partial}{\partial t} + (\mathbf{v} \cdot \nabla) . \tag{13}$$

Analogously to the dimensionless parameters in Zhang & Gubbins (1992), the Ekman number E, the Prandtl number P_r, the stratification parameter S_t and the buoyancy parameter B are defined by

$$E = \frac{\nu}{2\Omega d^2} , \quad P_r = \frac{\nu}{\kappa} , \quad S_t = \frac{\beta d}{\mathscr{H}} , \quad B = \frac{\mathscr{H} \alpha \gamma d^3}{2\Omega\kappa} . \tag{14}$$

Here, ν is the kinematic viscosity, Ω the angular velocity of the rotating frame and α the thermal expansivity. E primarily measures the rate of rotation, P_r the ratio of the thermal diffusion time to the viscous diffusion time, S_t the ratio of radial to lateral density gradients and B the strength of the laterally varying heat flux. As in Zhang & Gubbins (1992), most of the calculations were performed at infinite Prandtl number, although many calculations were also performed at $P_r = 1$ to confirm that retaining the non-linear inertial term in eq. (11) made no significant change to the solution.

The continuity equation,

$$\nabla \cdot \mathbf{v} = 0 , \tag{15}$$

allows the velocity, $\mathbf{v}$, to be written in terms of poloidal and toroidal scalar functions,

$$\mathbf{v} = \nabla \times \nabla \times [p(r, \theta, \phi)\mathbf{r}] + \nabla \times [\tau(r, \theta, \phi)\mathbf{r}] . \tag{16}$$

The impenetrable condition on $\mathbf{v}$ requires

$$p(r_i) = p(r_o) = 0 . \tag{17}$$

If the stress-free boundary condition is applied, the poloidal and toroidal scalars must satisfy

$$\left.\frac{\partial^2 p}{\partial r^2}\right|_{r_i, r_o} = \left.\frac{\partial}{\partial r}\left(\frac{\tau}{r}\right)\right|_{r_i, r_o} = 0 , \tag{18}$$

and if the rigid boundary is enforced, eq. (18) is replaced with the condition

$$\left.\frac{\partial p}{\partial r}\right|_{r_i, r_o} = \tau\Big|_{r_i, r_o} = 0 . \tag{19}$$

The lateral thermal anomaly at the outer surface of the spherical shell, $g(\theta, \phi)$, is expressed as a series of spherical harmonics,

$$g(\theta, \phi) = \sum_{l,m} (g_l^{mc} \cos m\phi + g_l^{ms} \sin m\phi) P_l^m(\cos\theta) , \tag{20}$$

where the associated Legendre functions $P_l^m(\cos\theta)$ are Schmidt quasi-normalized with

$$\int_{-\pi}^{\pi} [P_l^m(\cos\theta)]^2 \sin\theta d\theta = \frac{2(2 - \delta_{m0})}{2l + 1} . \tag{21}$$

The functions for $\Theta(r, \theta, \phi)$, $p(r, \theta, \phi)$ and $\tau(r, \theta, \phi)$ each have similar representations:

$$\Theta(r, \theta, \phi) = \sum_{l=0}^{L} \sum_{m=0}^{l} [\Theta_l^{mc}(r) \cos m\phi + \Theta_l^{ms}(r) \sin m\phi] P_l^m(\cos\theta) , \tag{22}$$

$$p(r, \theta, \phi) = \sum_{l=1}^{L} \sum_{m=0}^{l} [p_l^{mc}(r) \cos m\phi + p_l^{ms}(r) \sin m\phi] P_l^m(\cos\theta) , \tag{23}$$

$$\tau(r, \theta, \phi) = \sum_{l=1}^{L} \sum_{m=0}^{l} [\tau_l^{mc}(r) \cos m\phi + \tau_l^{ms}(r) \sin m\phi] P_l^m(\cos\theta) . \tag{24}$$

The spherical harmonics, Y_l^{mc} and Y_l^{ms}, are defined by

$$\begin{aligned} Y_l^{mc}(\theta, \phi) &= P_l^m(\cos\theta) \cos m\phi , \\ Y_l^{ms}(\theta, \phi) &= P_l^m(\cos\theta) \sin m\phi . \end{aligned} \tag{25}$$

The symmetry properties of eqs (11) and (12) allow for some subsets of the spherical harmonics in expansions (22), (23) and (24) to exist as self-consistent solutions, given appropriate boundary conditions. This is very advantageous when performing large, non-linear calculations as the reduced number of harmonics means that far finer spatial resolution (higher L) can be achieved for the same computational expense. All such symmetries are dealt with by Gubbins & Zhang (1993), whose notation is adopted here. A scalar function, s, which satisfies

$$s(\theta, \phi) = s(\pi - \theta, \phi) , \tag{26}$$

is equatorially symmetric and labelled E^S, as is a vector function, $\mathbf{S}=(S_r, S_\theta, S_\phi)$, which satisfies

$$[S_r, S_\theta, S_\phi](r, \theta, \phi)=[S_r, -S_\theta, S_\phi](r, \pi-\theta, \phi)\,. \tag{27}$$

Similarly, a scalar function, a, satisfying

$$a(\theta, \phi)=-a(\pi-\theta, \phi)\,, \tag{28}$$

and a vector function, $\mathbf{A}=(A_r, A_\theta, A_\phi)$, satisfying

$$[A_r, A_\theta, A_\phi](r, \theta, \phi)=[-A_r, A_\theta, -A_\phi](r, \pi-\theta, \phi)\,, \tag{29}$$

are equatorially antisymmetric and labelled E^A.

For an E^S heat flux pattern, $g(\theta, \phi)$, a solution $(\mathbf{v}, \Theta)$ driven by g need only consist of E^S components since no E^A components result from the non-linear interaction of E^S components. If, however, g is E^A, the solution must necessarily contain components of both symmetries as E^S components result from non-linear interaction of E^A components (see Gubbins & Zhang 1993). In addition, if m_0 is the highest integer such that

$$g(\theta, \phi)=g\left(\theta, \phi+\frac{2\pi}{m_0}\right)\,, \tag{30}$$

then the expansions for Θ, p and τ need only contain spherical harmonic components with m as an integer multiple of m_0.

Solutions to eqs (11) and (12) are sought with $\partial/\partial t=0$ using a Newton–Raphson-type iteration. The truncation parameter, L, was increased until the solutions ceased to be sensitive to further increases. Convergence was judged to occur at $L=L_c$ if the kinetic energy, integrated over the volume of the spherical shell, of the generated flows changed by less than 1 per cent for $L > L_c$. The total number of spherical harmonics required to represent the solution for a given L is denoted N_L. If no symmetry constraints are applied then $N_L=3L(L+2)$ and, although this number is greatly reduced by enforcing equatorial and/or rotational symmetry, in all cases N_L increases rapidly with L.

The radial functions in the series (22), (23) and (24) were represented at N_r equally spaced nodes and derivatives calculated by fourth-order finite differences. A suitable arrangement of the elements in the solution vector allows a band structure for the matrix used to solve eqs (11) and (12). The local nature of finite differences means the width of this matrix is constant for all N_r, so the size and computational cost of the problem increases only linearly with N_r. The spectral expansions used here are not local, so both dimensions of the matrix are proportional to N_L. As a consequence, increases in L cause a far greater increase in computational expense than increases in N_r.

The steady solutions, denoted by $\mathbf{v}_0$ and Θ_0, were subject to infinitesimal perturbations, $\tilde{\mathbf{v}}$ and $\tilde{\Theta}$, in order to determine their stability. Setting

$$\mathbf{v}=\mathbf{v}_0+\tilde{\mathbf{v}} \tag{31}$$

and

$$\Theta=\Theta_0+\tilde{\Theta}\,, \tag{32}$$

and assuming $\tilde{\mathbf{v}}$ and $\tilde{\Theta}$ to have an exponential time dependence of the form $\partial/\partial t=\sigma$ gives an eigenvalue problem

$$\begin{aligned}\sigma\frac{E}{P_r}\nabla\times\tilde{\mathbf{v}}=&-\frac{E}{P_r}\nabla\times[(\mathbf{v}_0\,.\,\nabla)\tilde{\mathbf{v}}+(\tilde{\mathbf{v}}\,.\,\nabla)\mathbf{v}_0]-\nabla\times(\mathbf{k}\times\tilde{\mathbf{v}})\\&+B\nabla\times(\tilde{\Theta}\mathbf{r})+E\nabla\times\nabla^2\tilde{\mathbf{v}}\,,\\ \sigma\tilde{\Theta}=&-S_t\tilde{\mathbf{v}}\,.\,\mathbf{r}-\mathbf{v}_0\,.\,\nabla\tilde{\Theta}-\tilde{\mathbf{v}}\,.\,\nabla(\Theta_0+fg)+\nabla^2\tilde{\Theta}\,.\end{aligned} \tag{33}$$

The eigenvalue $\sigma=\sigma_\mathrm{r}+i\sigma_\mathrm{i}$ is in general complex and an eigenvalue with real part $\sigma_\mathrm{r} < 0$ indicates that the steady solution is stable to perturbation and the steady solution is valid. An eigenvalue with $\sigma_\mathrm{r} > 0$ indicates that the perturbation would grow; the solution is therefore unstable so a full time integration would be needed to trace the evolution of the flow and temperature.

3 EFFECT OF VARYING THE EKMAN NUMBER

In the Earth, the Ekman number is anticipated to be between 10^{-11} and 10^{-15} (see e.g. Melchior 1986). However, such values cannot be approached numerically as boundary layers and internal shear layers form that require increasingly fine resolution as the rotation rate is increased (see Hollerbach 1994a,b). Even using hyperviscosities (see Zhang & Jones 1997) it is not generally possible to use values of E less than 10^{-6} with current numerical resources.

In the standard thermal convection problem with a uniformly heated boundary, the length scale of the flow is fundamentally determined by E, being of order $E^{1/3}$ (see e.g. Roberts 1968; Busse 1970). However, in the boundary-forced convection problem, the length scale of the flow is imposed by the lateral heat flux pattern (specified by $g(\theta, \phi)$), so a finite Ekman number may be able to represent the limit $E\to 0$ (Zhang & Gubbins 1992) whilst avoiding the numerical difficulties associated with high rotation speeds. The purpose of this section is to establish a value of E at which well-converged numerical solutions can be obtained, and below which the fundamental features of the driven flow do not change significantly.

Steady solutions were obtained for different values of E, using a Y_2^{2c} heat flux pattern, stress-free boundaries, zero mean radial temperature gradient ($S_t=0$) and low buoyancy number ($B=1$). Fig. 1(a) shows, at $E=10^{-1}$, upwellings (maximum negative $\partial v_r/\partial r$) in the equatorial plane to correspond to the maxima in the laterally varying temperature, T_1 ($\phi=0$ and $\phi=\pi$), and downwellings to maximum outward heat flux ($-\partial T_1/\partial r$) at $\phi=\pi/2$. The meridian sections show little evidence of the Taylor–Proudman theorem being satisfied by $\mathbf{v}$. In Fig. 1(b), the rotation is higher ($E=10^{-2}$) and the meridian section contour plots show greater alignment of the velocity features with the rotation axis, the v_r plot indicating the existence of a tangent cylinder over the inner core. The equatorial plots show an azimuthal shift of the alignment of maximum upwelling and maximum T_1.

At $E=10^{-3}$ in Fig. 1(c), this shift is increased with the region of maximum upwelling corresponding to $T_1=0$, where surface heat flux goes from negative to positive ($\phi\approx\pi/4$). This was also the case observed by Zhang & Gubbins (1992) in the high-rotation, $S_t=0$ and fixed-temperature calculations. The rotation axis alignment effects are also enhanced, with evidence of a Stewartson (1966) shear layer on the tangent cylinder. The $E=10^{-4}$ diagrams (Fig. 1d) show little qualitative difference from those at $E=10^{-3}$, except for greater shear around the tangent cylinder. In particular, the concentrations of the kinetic energy occur in the same locations relative to the imposed heat flux pattern.

Fig. 2 shows that an increase in rotation from $E=10^{-3}$ to $E=10^{-4}$ has little effect on the kinetic energy of the velocity components, except for the toroidal harmonics with high l. The

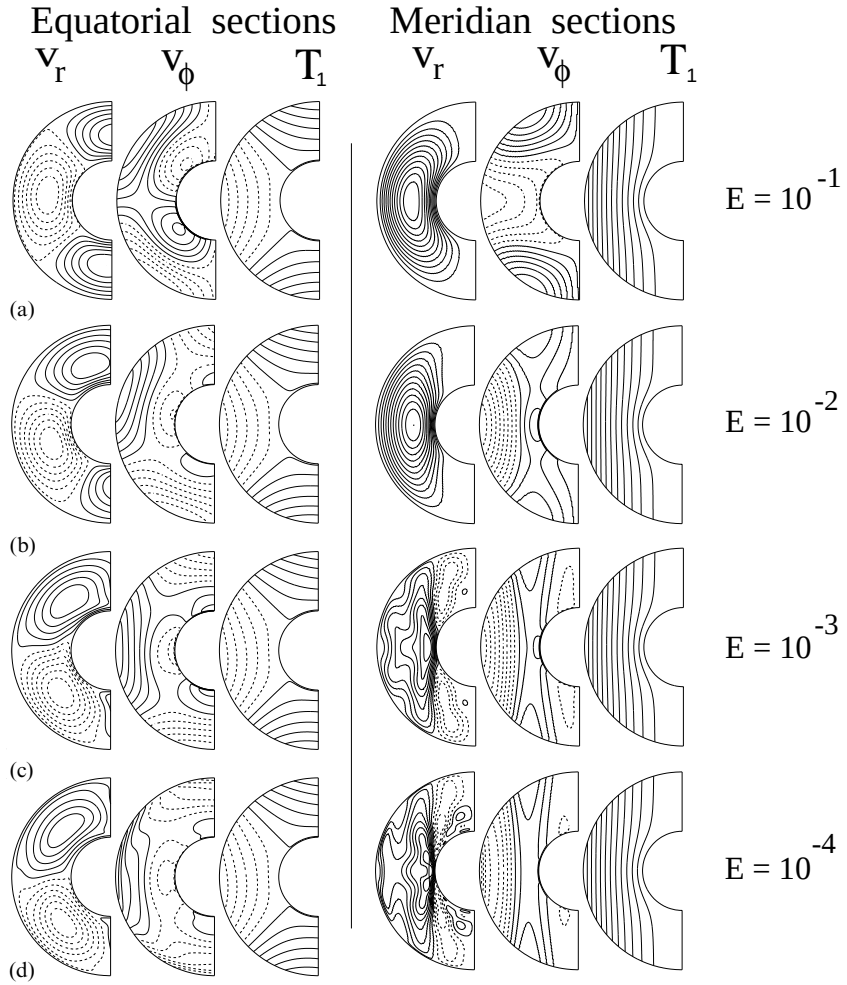

Figure 1. Steady solutions driven by a Y_2^{2c} boundary heat flux pattern with $B=1$, $S_t=0$ and stress-free boundaries. In each row, from left to right, the diagrams show contours of v_r, v_ϕ and T_1 (in the equatorial plane $\theta=\pi/2$, $0\le\phi\le\pi$) and v_r, v_ϕ and T_1 (in the meridian plane $\phi=0$, $0\le\theta\le\pi$). The Ekman number, E, takes the values 10^{-1} (row a), 10^{-2} (row b), 10^{-3} (row c) and 10^{-4} (row d). Contour levels vary between plots.

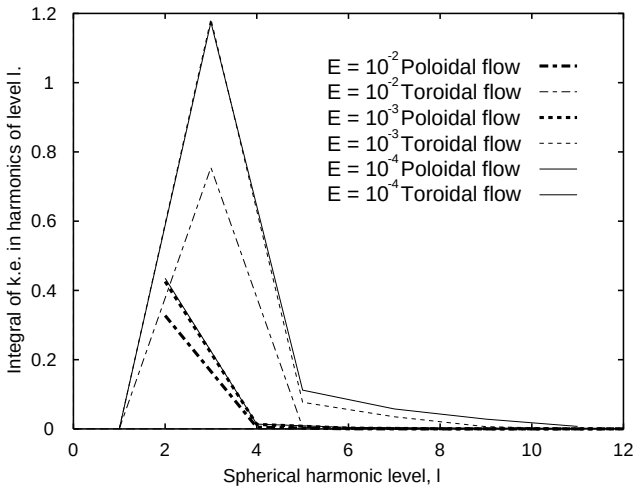

Figure 2. The kinetic energy of harmonics of level l in the velocity generated by a Y_2^{2c} boundary heat flux pattern, with $B=1$, $S_t=0$ and stress-free boundaries for three values of the Ekman number, $E=10^{-2}$, $E=10^{-3}$ and $E=10^{-4}$. Because of the symmetry of the flow, the poloidal harmonics have l even and the toroidal harmonics have l odd.

similar appearance of these boundary-driven flows (Figs 1c and d) and the kinetic energy spectra (Fig. 2) suggests that the flows are of a similar nature and differ only in the rotation-induced shear layers. The flow at $E=10^{-3}$ was considered to be adequately converged by $L_c=12$, whereas that at $E=10^{-4}$ required $L_c=18$, a far greater computational expense. Although far higher values were possible, $N_r=100$ was found to give adequate resolution in the radial direction for all parameters investigated. Since the difficulty of numerical representation lies in resolving the shear layers, whose behaviour is well understood (Stewartson 1966), there is deemed to be no useful purpose in running large, expensive calculations at faster rotation speeds; small decreases in E will result in far greater computational cost with limited returns.

Many calculations of Zhang & Gubbins (1992) were performed at $E=10^{-5}$ and the appearance of the flows obtained is similar to those presented here. Indeed, for some parts of the parameter space studied in this work, it is possible to obtain well-converged solutions at this value of E. However, the internal shear layers that result for other parameters cannot be adequately resolved at $E=10^{-5}$; a higher value of E is therefore used so that E can be held constant for all values of B and S_t investigated.

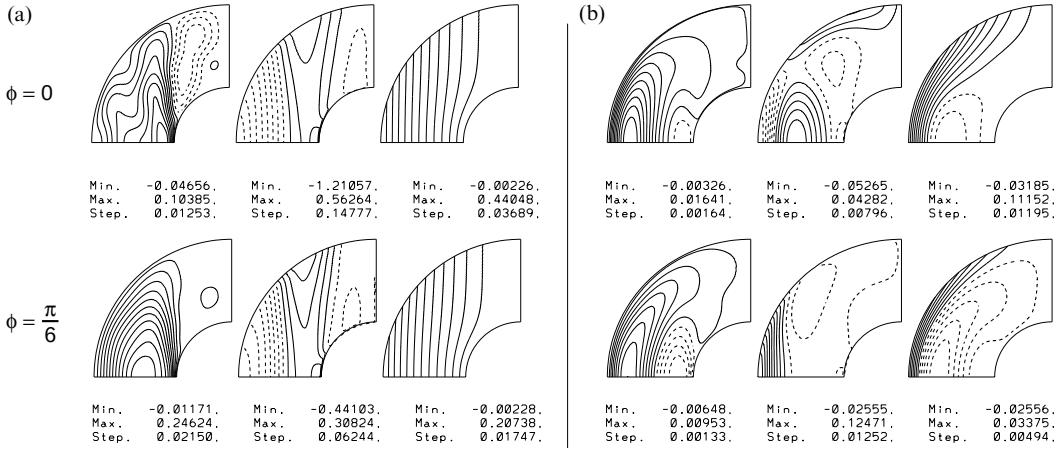

Figure 3. Steady solutions driven by a Y_2^{2c} surface heat flux anomaly with stress-free boundaries, $E = 10^{-3}$, $B = 1$ and infinite P_r shown in meridian section. (a) The solution at $S_t = 0$ and (b) the solution at $S_t = 100$. For each row, the left, centre and right-hand plots show respectively contours of v_r, v_ϕ and T_1 in the meridian plane with $0 \leq \theta \leq \pi/2$. (The equatorial symmetry of the solutions only requires this half-plane to be shown.) The azimuthal value for each row is given at the side. Contours are evenly spaced between the limits shown, with negative numbers being represented by dashed contour lines.

It will be assumed that, for such boundary-driven flows, $E = 10^{-3}$ will give a qualitatively accurate approximation of the $E \to 0$ limit, whilst allowing flows to be fully resolved at moderate computational cost.

4 THE EFFECT OF STABLE DENSITY STRATIFICATION

4.1 Equatorially symmetric heat flux patterns

The imposition of stable stratification was shown by Zhang & Gubbins (1992) to cause some confinement of the driven flows to the outside of the shell, although to a far lesser extent than would be expected without the influence of the Coriolis force. Calculations with a fixed surface heat flux (as opposed to temperature) show a very similar phenomenon. A lateral heat flux variation, $g(\theta, \phi)$, was prescribed with a Y_2^{2c} form. Fig. 3 shows how stable stratification breaks down the axial velocity structures that result from the high rotation rate, resulting in a shift of kinetic energy from the centre to the periphery of the shell.

Fig. 4 displays the change in the azimuthal relationship between the concentration of kinetic energy and the applied heat flux when stable density stratification is applied. In Fig. 4(b), a much weakened upwelling occurs directly below a region of high temperature, as in the case of low rotation speed displayed in Fig. 1(a). Stable stratification not only reduces the penetration of flow but also suppresses the effect of the Coriolis force on the resulting velocity.

The effect of the length scale of the applied lateral heat flux variation was also investigated and, like the Zhang & Gubbins (1992) fixed-temperature calculations, the flow driven by a Y_8^8 heat flux pattern was found to penetrate less deeply into the shell. Fig. 5 shows how, although the flow driven by the small length scale heating mode is less energetic than that driven by the large-scale heat flux pattern, being a more local

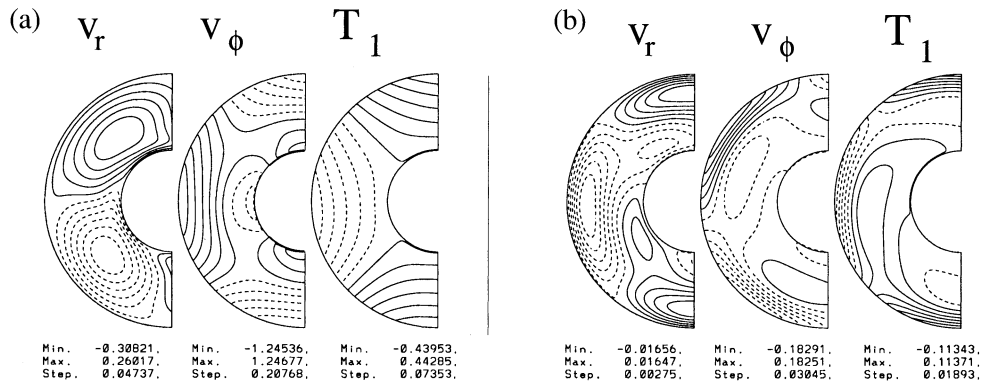

Figure 4. Steady solutions driven by a Y_2^{2c} surface heat flux anomaly with stress-free boundaries, $E = 10^{-3}$, $B = 1$ and infinite P_r shown in equatorial section. (a) The solution at $S_t = 0$ and (b) the solution at $S_t = 100$. Contours of v_r, v_ϕ and T_1 are shown in the meridian plane with $0 \leq \phi \leq \pi$ and $\theta = \pi/2$. Contours are evenly spaced between the limits shown, with negative numbers being represented by dashed contour lines.

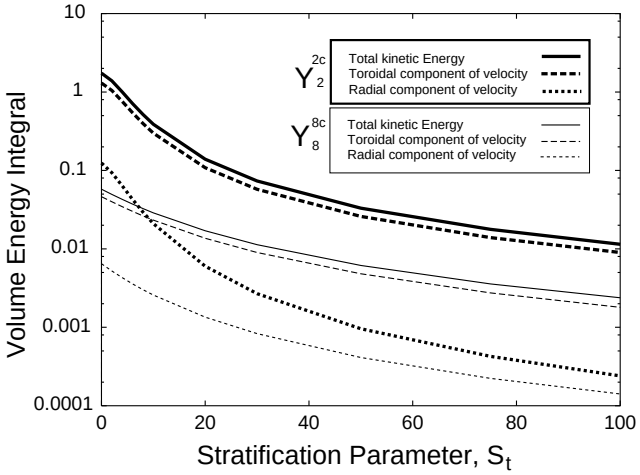

Figure 5. The kinetic energy integrated over the spherical shell, as a function of S_t for velocities driven by a Y_2^{2c} and a Y_8^{8c} fixed heat flux outer boundary condition. $E=10^{-3}$, $B=1.0$ and boundaries are stress free.

phenomenon, it is rather less inhibited by the stable stratification. Consequently, given a heat flux variation over the surface containing different length scales, the effect of the small length scale variations will be relatively greater in a stratified fluid.

The normalization condition (6) is recalled that ensures that the mean square heat flux variation is identical for the Y_2^{2c} and Y_8^{8c} modes. The difference in behaviour must therefore be attributed to the difference in lateral length scale alone. Maintaining the mean square heat flux is achieved by manipulating the coefficients g_l^{mc} and g_l^{ms} in eq. (20). For example, if g takes on a Y_2^{2c} lateral variation, $g_2^{2c}=\sqrt{5/(4\pi)}$ will give the same mean square lateral heat flux variation as a Y_8^{8c} pattern with $g_8^{8c}=\sqrt{17/(4\pi)}$.

The use of rigid, as opposed to stress-free, boundaries made little difference to the appearance of the flows. For the same governing parameters, E, P_r, S_t, B and g, flow penetrates slightly deeper into the shell when a rigid boundary is specified because the fixed heat flux boundary condition demands that the same bulk of heat is transferred laterally and the no-slip condition resists flow near the boundary, forcing the flow further into the shell.

4.2 Equatorially antisymmetric heat flux patterns

The lateral variation in heat flux at the CMB will almost certainly not satisfy a strict equatorial symmetry, so the effect of equatorially antisymmetric (E^A) heat flux patterns must also be understood. Zhang & Gubbins (1992) anticipated a different behaviour for E^A temperature variations due to the nature of the Coriolis force, but were unable to pursue these calculations due to the increased computational expense. Fig. 6 shows the resulting flow and temperature distributions when the sphere is subjected to a large-scale E^A surface heat flux pattern. Only meridian sections are shown as the kinetic energy contained in E^S components is found to be very small and equatorial section diagrams would therefore not be very informative. It is, however, clear from the meridian sections that a twist in azimuth of the flow relative to the thermal boundary condition has been caused by the stable stratification.

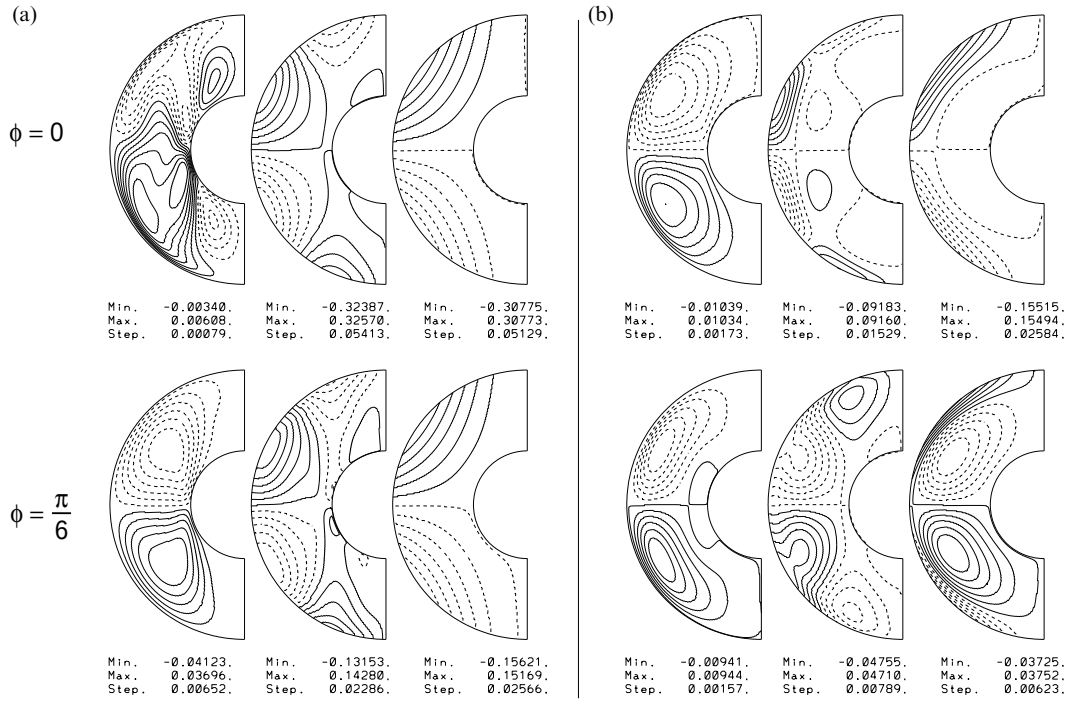

Figure 6. Steady solutions driven by a Y_3^{2c} surface heat flux anomaly with stress-free boundaries, $E=10^{-3}$ and $B=1$ shown in meridian section. (a) The solution at $S_t=0$ and (b) the solution at $S_t=100$. For each row, the left, centre and right-hand plots show respectively contours of v_r, v_ϕ and T_1 in the meridian plane with $0\leq\theta\leq\pi$. The azimuthal value for each row is given at the side. Contours are evenly spaced between the limits shown, with negative numbers being represented by dashed contour lines.

The axial shear structures associated with the high rotation speed, which occur when the flow is driven by an E^S heat flux inhomogeneity (see especially Figs 1c and d), are far less apparent. The flow is primarily constrained by the opposing thermal forcing above and below the equatorial plane. Although there is evidence of a shift of kinetic energy away from the inner surface, it is far less significant than for the E^S case: compare the difference in plots (a) and (b) between Figs 3 and 6.

The different extent to which stable stratification affects E^S and E^A boundary-driven flows is clarified by comparing the kinetic energies of flows. Fig. 7 shows how, in the neutrally stable case, the flow driven by the Y_3^{2c} heat flux pattern is more than an order of magnitude less energetic than that driven by the Y_2^{2c} pattern. As S_t is increased, however, the decline in energy is far slower for the E^A mode than the E^S. With $S_t \geq 50$, there is almost no difference between the energy of the different flows, regardless of the smaller lateral length scale of the anti-symmetric heat flux variation. It is also noted that the Y_3^{2c} flow is almost entirely toroidal for all values of S_t.

4.3 Heat flux patterns containing both equatorially symmetric and antisymmetric components

To study the behaviour of flows where symmetric and antisymmetric components may interact, the inhomogeneity function, g, is defined by

$$g(\theta, \phi) = \frac{\sqrt{\frac{5}{4\pi}}\, Y_2^{2c}(1-\alpha) + \sqrt{\frac{7}{4\pi}}\, Y_3^{2c}\alpha}{\sqrt{1-2\alpha(1-\alpha)}}\,. \tag{34}$$

The driving heat flux pattern is entirely E^S when $\alpha = 0$ and entirely E^A when $\alpha = 1$. Fig. 8 shows, as a function of α and S_t, the proportion of kinetic energy in the resulting flows that is attributable to E^A velocity components.

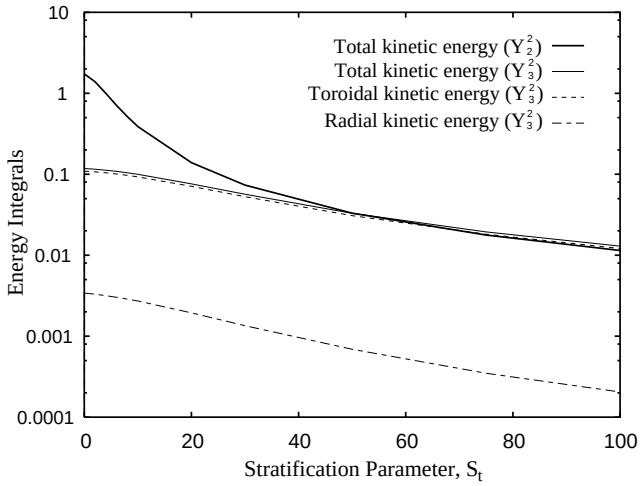

Figure 7. Kinetic energy of radial, toroidal and total velocity components driven by a Y_3^{2c} boundary heat flux, as a function of S_t with $E = 10^{-3}$, $B = 1.0$ and stress-free boundaries. For the purpose of comparison, the total kinetic energy curve for the Y_2^{2c} surface heat flux, taken from Fig. 5, is also shown.

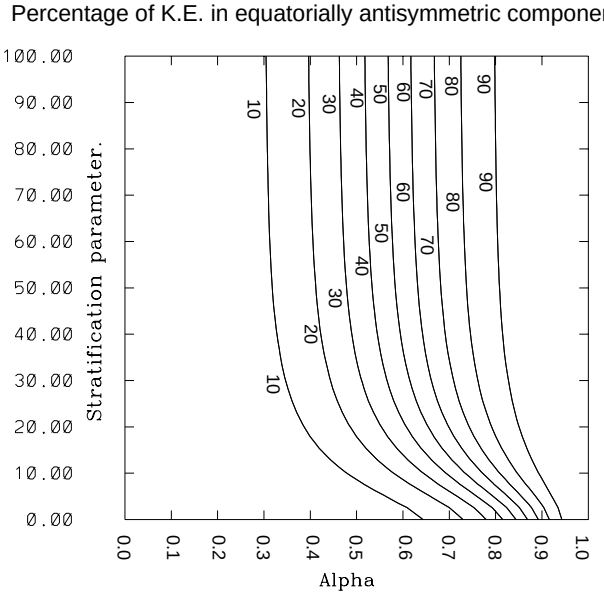

Figure 8. Percentage of kinetic energy in E^A velocity components as a function of S_t and α, a parameter controlling the relative strength of the E^S and E^A components of the imposed heat flux pattern. $g(\theta, \phi)$ is entirely E^S (E^A) when $\alpha = 0$ ($\alpha = 1$). $E = 10^{-3}$, $B = 1$ and boundaries are stress free.

The E^A contribution is greater for stable stratification than for the neutrally stable case for almost all values of α. The effect is significant: for a heat flux pattern, g, whose E^A components account for 70 per cent of the total heat transfer, less than 20 per cent of the resulting flow is in E^A components when $S_t = 0$ compared to over 70 per cent as S_t increases beyond 50. The E^A contribution to the applied heat flux variation has to be quite substantial before significant E^A components are found in the driven flow. This is probably a result of the larger lateral length scale of the Y_2^{2c} distribution.

The actual pattern of lateral variations in the CMB heat flux can, in principle, be determined from seismology if the variations of seismic velocity are caused by temperature rather than composition. Regions in the lowermost mantle of relatively fast (slow) seismic waves indicate lower (higher) temperatures in the thermal boundary layer and therefore higher (lower) core-to-mantle heat flow. A linear correlation will be assumed (see e.g. Yuen *et al.* 1993; Yuen *et al.* 1996) between lateral shear wave anomalies and the lateral variation in heat flux,

$$g(\theta, \phi) = C\,\frac{\delta v_s}{v_s}\,, \tag{35}$$

where v_s is the velocity of shear waves in the lowermost mantle and C is a constant of proportionality. A similar approach was employed by Olson & Glatzmaier (1996) and Glatzmaier & Roberts (1997). The SH10c17 model of Masters *et al.* (1992) gives lateral variation in $\delta v_s / v_s$ as an expansion of spherical harmonics to degree and order 10, and is displayed in Fig. 9(b). This spatial form was applied to the function g, and the resulting flows just below the outer surface are shown in Figs 9(a) and (c) for different values of B and S_t.

Fig. 9(a) shows flow just below the outer surface when subjected to the heat flux pattern in Fig. 9(b) with the parameters $B = 1$, $S_t = 1$, $E = 10^{-3}$ and infinite P_r. The flow is highly

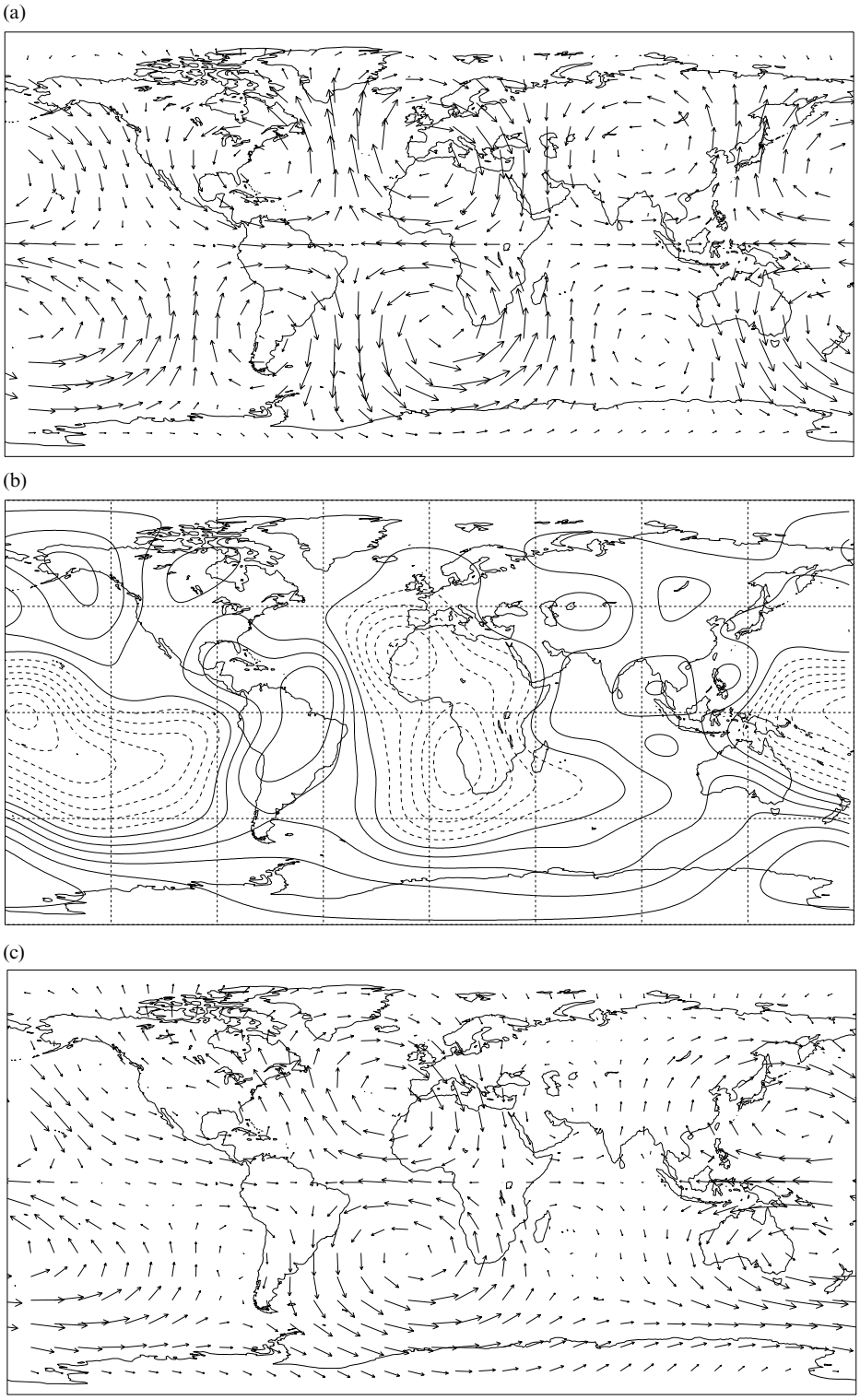

Figure 9. Surface flows obtained assuming a linear relation between $\delta v_s/v_s$ in the lowermost mantle and lateral heat flux variation across the CMB. $g(\theta, \phi)$ is prescribed as the SH10c17 ($\delta v_s/v_s$) model of Masters *et al.* (1992) shown in (b) with solid lines indicating high v_s (maximum $+1.48$ per cent) and dashed lines indicating low v_s (minimum -1.83 per cent). (a) The surface flow obtained with $B=1$, $S_t=1$ and $E=10^{-3}$ and (c) the flow obtained with $B=2$, $S_t=40$ and $E=10^{-3}$. Stress-free boundaries are employed in both calculations. Lengths of arrows indicate the flow strengths and are drawn to the same scale in (a) and (c).

equatorially symmetric and bears great resemblance to that driven by the Y_2^{2c} surface harmonic in this parameter range. Flow below the Atlantic Ocean is dominated by strong poleward currents and, due to the low value of the stratification parameter, the flow penetrates to the bottom of the spherical shell and as such is dominated by rotational effects and is not consistent with horizontal flow in a density stratified layer at the top of the core.

Fig. 9(b) shows the surface flow that results when $B=2$ and $S_t=40$. The flow is noticeably less energetic and the departures from equatorial symmetry are far greater. The stratification has broken the effects of the rotation, and flow below the Atlantic now displays westward flow at the equator and gyres in the Northern and Southern Hemispheres. These features share some similarity in form to those of flows calculated by inversion from data for geomagnetic secular variation (see Bloxham & Jackson 1991 for a review).

5 CONCLUSIONS

Applying an inhomogeneous heat flux to the surface of a rotating spherical fluid shell drives a steady flow in the cases of neutral and stable stratification. Increasing the rotation speed causes the locations of upwelling and downwelling to shift relative to the applied thermal heterogeneity. With E below 10^{-3}, little change in the large-scale flow was observed, although increasing difficulty in representing the tangential shear layers made numerical calculations more computationally expensive. $E=10^{-3}$ was judged to be a reasonable limit of high rotation at which further calculations could be carried out with good numerical convergence.

Density stratification was included in the model by a parameter S_t, which controlled a subadiabatic temperature gradient. With $S_t=0$, the flow driven by large-scale E^S heat flux patterns penetrated the depth of the spherical shell and had significant radial components. The flow is dominated by rotation with shear on the tangent cylinder to the inner core. As S_t is increased, the effect of the rotation is reduced and the kinetic energy diminishes, flow becoming confined to near the boundaries. The radial component rapidly decreases and the flow becomes predominantly toroidal. Smaller length-scale E^S heat flux variations (Y_8^8 was used) drive less energetic flows that do not penetrate so deeply. All these flows are very similar to those obtained by fixing the surface temperature.

Equatorially anti-symmetric (E^A) heat flux distributions were also applied. With $S_t=0$, large-scale heat flux patterns drive flows with far less kinetic energy than the E^S boundary heat flux; the flow is mainly toroidal and less dominated by the rotation. An increase in the stratification parameter again reduces the kinetic energy and shifts flow towards the boundaries, although the effect on the flow is far smaller than for the E^S case.

E^S solutions are normally favoured energetically because structures that are aligned along the rotation axis by the Proudman–Taylor theorem are larger scale than the corresponding E^A structures, which must change sign at the equator. When the flows are confined to the surface by stratification there is no connection between the two hemispheres, and the rotation exerts no preference of symmetry. In general the boundary heat flux will contain both E^S and E^A components. We expect the E^S symmetry to dominate the flow for neutral stability, and this proved to be the case for the general model based on a lowermost mantle shear wave model in Section 4.3.

The form of the boundary-driven flows was not significantly changed by imposing a fixed inhomogeneous heat flux as opposed to temperature. Zhang & Gubbins (1992) argued that this would be the case, although stating that they would be unable to show that the two types of solution had the same stability properties. All solutions reported in this paper are steady and stable to perturbation. However, increasing the buoyancy number, B, causes the isotherms to distort as smaller-scale convective motions result from the increased non-linearity of the solutions. This demands greater lateral resolution with correspondingly higher computational cost. The appearance of the flows suggests that a continual increase in the strength of the lateral heat flux variation will lead to an unstable or time-dependent flow, although no positive perturbation growth rate was found that converged with increasing numerical resolution. Specifying a fixed heat flux instead of temperature in the unstable, uniform thermal boundary problem has a very significant effect on the preferred mode of flow for a given rotation speed (Gibbons 1998) and the behaviour in the (unstable) inhomogeneous heat flux system is directly related to the linear stability problem (manuscript in preparation).

The solutions obtained when boundaries were rigid also differed only slightly from the stress-free solutions, mainly in the depth to which flow penetrated as the stratification parameter was increased. This is in contrast to the case of flow in uniformly heated spheres and shells, where changing the viscous boundary condition has long been known to alter flow significantly (Chandrasekhar 1961; Roberts 1968). The viscous boundary condition also has a significant effect on the magnetic field in dynamo calculations (Kuang & Bloxham 1997).

Solutions calculated at $P_r=1$ showed no qualitative difference to those displayed at infinite P_r. This is in contrast to the uniform thermal boundary case (Zhang & Busse 1987; Zhang & Jones 1993), where the Prandtl number is of fundamental importance in determining the preferred mode of solution. When the free convection with inhomogeneous temperature boundary condition calculations are performed at finite Prandtl number (Zhang & Gubbins 1996), the ability of the temperature heterogeneity to lock the drifting flow is strongly reduced.

Our main result, that the core may respond predominantly to the E^S part of the boundary heat flux variation, may have significant implications for the secular variation. However, the model is much too simple to apply directly to the Earth. Making a serious attempt to apply the model reveals two distinct difficulties: how to estimate the CMB heat flux from shear wave speed, and how to model the core dynamics.

CMB heat flux must be estimated in three stages. First, we convert seismic velocity to temperature using a simple linear relation. Second, we ascribe that temperature to a thermal boundary layer at the base of the mantle whose thickness is determined by the resolution of the seismic data. Third, we use the temperature across the boundary layer to estimate the heat flux on the basis that the CMB itself is almost isothermal.

Lateral variations in heat flux will exhibit the same pattern as that of the shear wave velocity, provided that seismic variations are controlled by temperature and not, for example, by composition. [Robertson & Woodhouse (1996) and Su & Dziewonski (1997) suggested that negative correlations in P- and S-wave velocity variations indicate strong compositional heterogeneity in the lowermost mantle.] The origin of lower mantle heterogeneities is an active research area and there is continual improvement in the understanding of the role played by compositional variations in the lower mantle. The amplitudes of the heat flux variations, however, depend on very poorly known quantities such as the thickness of the thermal boundary layer. Models of lower mantle convection are needed to improve our understanding of this boundary layer. The buoyancy parameter, B, in eq. (14) also depends upon the thermal expansion and conductivity of core iron, both poorly

known parameters. Furthermore, it is necessary here, as for geodynamo studies, to use a turbulent value of the thermal diffusivity that is many orders of magnitude greater than the molecular value. It will therefore be very difficult to estimate *B a priori.* Rather, future estimates of this parameter will come from comparing model results with the observed secular variation.

Turning to core dynamics, the greatest unknown is probably the correct value and nature of the turbulent thermal diffusivity. Even turbulent diffusivities allow values of B far greater than used here, into regimes where the flows considered here would be unstable. In addition, the core will be mostly, if not entirely, convective, with competition between boundary-driven flow and convection driven by buoyancy sources at the inner core boundary.

ACKNOWLEDGMENTS

We are very grateful to K. Zhang for useful discussions on this work and to T. G. Masters for the shear wave model. We also wish to thank M. Kendall for discussions on seismic heterogeneity at the base of the mantle. SJG was supported by a NERC PhD studentship. The work was also supported by NERC grant GR3/09741 and by PPARC grant GR/L22973.

REFERENCES

Bassom, A.P. & Soward, A.M., 1996. Localised rotating convection induced by topography, *Physica D,* **97,** 29–44.

Bell, P.I. & Soward, A.M., 1996. The influence of surface topography on rotating convection, *J. Fluid Mech.,* **313,** 147–180.

Bloxham, J. & Gubbins, D., 1987. Morphology of the geomagnetic field and implications for the geodynamo, *Nature,* **325,** 509–511.

Bloxham, J. & Jackson, A., 1991. Fluid-flow near the surface of Earth's outer core, *Rev. Geophys.,* **29,** 97–120.

Bloxham, J., Gubbins, D. & Jackson, A., 1989. Geomagnetic secular variation, *Phil. Trans. R. Soc. Lond.,* A**329,** 415–502.

Braginskii, S.I., 1984. Short period geomagnetic secular variation, *Geophys. Astrophys. Fluid Dyn.,* **30,** 1–78.

Braginskii, S.I., 1993. MAC-Oscillations of the hidden ocean of the core, *J. Geomag. Geoelectr.,* **45,**

Busse, F.H., 1970. Thermal instabilities in rapidly rotating systems, *J. Fluid Mech.,* **44,** 441–460.

Chandrasekhar, S., 1961. *Hydrodynamic and hydromagnetic stability,* Clarendon Press, Oxford.

Davis, R.G. & Whaler, K.A., 1993. Velocity fields at the Earth's core surface from 1900 to 1980 using the frozen-flux approximation and steady velocity assumption, *Geophys. Astrophys. Fluid Dyn.,* **67,** 241–258.

Fearn, D.R. & Loper, D.E., 1981. Compositional convection and stratification of the Earth's core, *Nature,* **289,** 393–394.

Glatzmaier, G.A. & Roberts, P.H., 1997. Simulating the geodynamo, *Contemporary Phys.,* **38,** 269–288.

Gibbons, S.J., 1998. Dynamo models for the Earth's magnetic field, *PhD thesis,* University of Leeds.

Gubbins, D., 1991. Dynamics of the secular variation, *Phys. Earth planet. Inter.,* **68,** 170–182.

Gubbins, D. & Kelly, P., 1993. Persistent patterns in the geomagnetic field over the past 2.5 Myr, *Nature,* **365,** 829–832.

Gubbins, D. & Richards, M., 1986. Coupling of the core dynamo and mantle: thermal or topographic?, *Geophys. Res. Lett.,* **13,** 1521–1524.

Gubbins, D. & Roberts, P.H., 1987. Magnetohydrodynamics of the Earth's core, Chapter 1, in *Geomagnetism,* Vol. II, pp. 1–183, ed. Jacobs, J.A., Academic Press, New York.

Gubbins, D. & Zhang, K., 1993. Symmetry properties of the dynamo equations for paleomagnetism and geomagnetism, *Phys. Earth planet. Inter.,* **75,** 225–241.

Gubbins, D., Thomson, C.J. & Whaler, K.A., 1982. Stable regions in the Earth's liquid core, *Geophys. J. R. astr. Soc.,* **68,** 241–251.

Hide, R., 1967. Motions of the Earth's core and mantle, and variations of the main geomagnetic field, *Science,* **157,** 55–56.

Hide, R., 1969. Interaction between the Earth's liquid core and solid mantle, *Nature,* **222,** 1055–1056.

Hollerbach, R., 1994a. Imposing a magnetic field across a non-axisymmetric shear-layer in a rotating spherical shell, *Phys. Fluids,* **6,** 2540–2544.

Hollerbach, R., 1994b. Magnetohydrodynamic Ekman and Stewartson layers in a rotating spherical shell, *Phil. Trans. R. Soc. Lond.,* A**444,** 333–346.

Hutcheson, K. & Gubbins, D., 1990. A model of the geomagnetic field for the 17th century, *J. geophys. Res.,* **95,** 10 769–10 781.

Jeanloz, R., 1990. The nature of the Earth's core, *Ann. Rev. Earth planet. Sci.,* **18,** 357–386.

Johnson, C. & Constable, C., 1995. The time-averaged geomagnetic field as recorded by lava flows over the past 5 Myr, *Geophys. J. Int.,* **122,** 489–519.

Knittle, E. & Jeanloz, R., 1991. Earth's core-mantle boundary: results of experiments at high pressures and high temperatures, *Science,* **251,** 1438–1443.

Kuang, W. & Bloxham, J., 1997. An Earth-like numerical dynamo model, *Nature,* **389,** 371–374.

Labrosse, S., Poirier, J.P. & Le Mouël, J.L., 1997. On cooling of the Earth's core, *Phys. Earth planet. Inter.,* **99,** 1–17.

Lay, T. & Young, C.J., 1990. The stably-stratified outer core revisited, *Geophys. Res. Lett.,* **17,** 2001–2004.

Le Mouël, J.L., 1984. Outer core geostrophic flow and secular variation of the Earth's magnetic field, *Nature,* **311,** 734–735.

Li, X. & Jeanloz, R., 1987. Measurement of the electrical conductivity of [Mg, Fe] SiO_3-perovskite and a perovskite-dominated assemblage at lower mantle conditions, *Geophys. Res. Lett.,* **95,** 5067–5078.

Lister, J.R. & Buffett, B.A., 1998. Stratification of the outer core at the core-mantle boundary, *Phys. Earth planet. Inter.,* **105,** 5–19.

Lloyd, D.B. & Gubbins, D., 1990. Toroidal fluid motions at the top of the Earth's core, *Geophys. J. R. Astr. Soc.,* **100,** 455–467.

Masters, T.G., 1979. Observational constraints on the chemical and thermal structure of the Earth's deep interior, *Geophys. J. R. astr. Soc.,* **57,** 507–534.

Masters, T.G., Bolton, H.F. & Shearer, P.M., 1992. Large-scale 3-dimensional structure of the mantle, *EOS, Trans. Am. geophys. Un.,* **73,** 201.

Melchior, P., 1986. *The Physics of the Earth's Core—An Introduction,* Pergammon Press, Oxford.

Olson, P. & Glatzmaier, G., 1996. Magnetoconvection and thermal coupling of the Earth's core and mantle, *Phil. Trans. R. Soc. Lond.,* A**354,** 1413–1424.

Poirier, J.P., Malavergne, V. & Le Mouël, J.L., 1998. Is there a thin electrically conducting layer at the base of the mantle?, in *The Core-Mantle Boundary Region,* pp. 131–137, eds Gurnis, M., Wysession, M.E., Knittle, E. & Buffett, B.A., AGU, Washington.

Roberts, P.H., 1968. On the thermal instability of a rotating fluid sphere containing heat sources, *Phil. Trans. R. Soc. Lond.,* A**263,** 93–117.

Robertson, G.S. & Woodhouse, J.H., 1996. Ratio of relative S to P wave velocity heterogeneities in the lower mantle, *J. geophys. Res.,* **101,** 20 041–20 052.

Sarson, G.R., Jones, C.A. & Longbottom, A.W., 1997. The influence of boundary region heterogeneities on the geodynamo, *Phys. Earth planet. Inter.,* **101,** 13–32.

Stacey, F.D., 1991. Effects on the core of structure within D'', *Geophys. Astrophys. Fluid Dyn.,* **60,** 157–163.

Stewartson, K., 1966. On almost rigid rotations (Part 2), *J. Fluid Mech.,* **26,** 131–144.

Su, W.J. & Dziewonski, A.M., 1997. Simultaneous inversion for 3-D variations in shear and bulk velocity in the mantle, *Phys. Earth planet. Inter.,* **100,** 134–156.

Sun, Z.P., Schubert, G. & Glatzmaier, G.A., 1994. Numerical simulations of thermal convection in a rapidly rotating spherical shell cooled inhomogeneously from above, *Geophys. Astrophys. Fluid Dyn.,* **75,** 199–226.

Whaler, K.A., 1980. Does the whole of the Earth's core convect?, *Nature,* **287,** 528–530.

Whaler, K.A., 1984. Fluid upwelling at the core–mantle boundary—resolvability from surface geomagnetic data, *Geophys. J. R. astr. Soc.,* **78,** 453–473.

Whaler, K.A., 1986. Geomagnetic evidence for fluid upwelling at the core–mantle boundary, *Geophys. J. R. astr. Soc.,* **86,** 563–588.

Yuen, D.A., Čadek O., Chopelas, A. & Matyska, C., 1993. Geophysical inferences of thermal-chemical structures in the lower mantle, *Geophys. Res. Lett.,* **20, 899–902.**

Yuen, D.A., Čadek, O., van Keken, P., Reuteler, D.M., Kyvalova, H. & Schroeder, B.A., 1996. Combined results from mineral physics, tomography and mantle convection and their implications on global geodynamics, in *Seismic Modelling of Earth Structure,* pp. 463–505, eds Boschi, E., Ekström, G. & Morelli, A., Instituto Nazionale di Geofisica, Rome.

Zhang, K. & Busse, F.H., 1987. On the onset of convection in rotating spherical shells, *Geophys. Astrophys. Fluid Dyn.,* **39,** 119–147.

Zhang, K. & Gubbins, D., 1992. On convection in the Earth's core driven by lateral temperature variations in the lower mantle, *Geophys. J. Int.,* **108,** 247–255.

Zhang, K. & Gubbins, D., 1993. Convection in a rotating spherical fluid shell with an inhomogeneous temperature boundary condition at infinite Prandtl number, *J. Fluid Mech.,* **250,** 209–232.

Zhang, K. & Gubbins, D., 1996. Convection in a rotating spherical fluid shell with an inhomogeneous temperature boundary condition at finite Prandtl number, *Phys. Fluids,* **8,** 1141–1148.

Zhang, K. & Jones, C., 1993. The influence of Ekman boundary layers on rotating convection, *Geophys. Astrophys. Fluid Dyn.,* **71,** 145–162.

Zhang, K. & Jones, C., 1997. The effect of hyperviscosity on geodynamo models, *Geophys. Res. Lett.,* **24,** 2869–2872.